Journal of Materials Science & Technology 194 (2024) 51–62

Contents lists available at ScienceDirect

Journal of Materials Science & Technology

journal homepage: www.elsevier.com/locate/jmst

Research Article

Enhanced plasticity in refractory high-entropy alloy via multicomponent ceramic nanoparticle

Hongyi Li[a,b], Fuhua Cao[a], Tong Li[a], Yuanyuan Tan[a], Yan Chen[a,b], Haiying Wang[a,b], Peter K. Liaw[c,*], Lanhong Dai[a,b,*]

[a] State Key Laboratory of Nonlinear Mechanics, Institute of Mechanics, Chinese Academy of Sciences, Beijing 100190, China
[b] School of Engineering Science, University of Chinese Academy of Sciences, Beijing 101408, China
[c] Department of Materials Science and Engineering, The University of Tennessee, Knoxville, TN 37996-2100, USA

ARTICLE INFO

Article history:
Received 18 October 2023
Revised 20 December 2023
Accepted 9 January 2024
Available online 28 February 2024

Keywords:
Refractory high-entropy superalloys
Plasticity
Multicomponent ceramic nanoparticles
Ordering-disordering transition

ABSTRACT

Refractory high-entropy alloys (RHEAs) exhibit remarkable strengths at elevated temperatures and are hence extremely promising candidates for high-temperature structural materials. However, the RHEAs with ordered superlattice structures generally suffer from poor room-temperature plasticity, which severely hampers their widespread applications. Here, we discovered that the introduction of multicomponent ceramic nanoparticles (MCNPs) into the RHEAs makes the problem alleviative and realizes a multifold increase in plasticity without sacrificing strength. The detailed characterizations show that the improvement originates from the chemical ordering-disordering transition near MCNPs in the B2-ordered RHEAs. This transition promotes the formation of local disordered regions where the mobility of dislocations is significantly enhanced. These regions wrap around MCNPs to form a unique heterogeneous structure, which suppresses the premature microcracks by the boosted dislocation mobility. Simultaneously, the existence of stable MCNPs prevents grain coarsening at elevated temperatures by Zener pinning. These novel alloy-design ideas shed new insights into developing RHEAs with an outstanding combination of strength and plasticity.

1. Introduction

Over the past decades, increasing operating temperatures have remained an essential way to improve efficiency and maximize thrust in the design of aerospace and gas turbine engines [1–3]. Therefore, it is of great significance to develop metallic materials for higher-temperature applications. Currently, Ni-based superalloys with a combination of properties are qualified for the role. In this kind of superalloy, the precipitation with a long-range ordered structure, i.e., an $L1_2$ structure, serves an essential duty in realizing high strengths in extreme conditions owing to strong chemical binding and low atomic mobility [4]. However, most of the beneficial structures annihilate at elevated temperatures and do not provide support for ultrahigh-temperature applications [5–7].

Traditional refractory alloys, albeit with the development potential due to high melting points, are generally insufficient in strength and high in density [1,8]. Hence, they are unsuitable for serving in the critical parts of air/aero vehicles. By copying the microstructure of the superalloy into the refractory alloys with a body-centered cubic (BCC) structure, the elegant integration of both advantages was accomplished by Naka et al. [9,10]. This category of refractory alloys with a BCC + B2 superstructure is found in highly alloyed systems, such as $AlNbTaTi_2$. It is noted that the ordered structure, i.e., B2, is extremely difficult to form in binary alloys [10–12]. Highly alloying refractory alloys, not built with one principal element and adding dilute concentrations of alloying elements, are based on a mixture of multiple refractory elements with similar atomic proportions, termed refractory high-entropy alloys (RHEAs) or refractory complex concentrated alloys (RCCAs) [13–30]. Recently, driven by this concept, a typical RHEA $AlMo_{0.5}NbTa_{0.5}TiZr$ with both BCC cuboidal nanoprecipitation and thin continuous B2 channels was successfully synthesized by Senkov et al. [31,32]. The RHEAs display an ultrahigh yield strength of ~ 750 MPa at 1000 °C [32]. It has surpassed all Ni-based superalloys and seems to be a strong candidate for high-temperature structural material. Nevertheless, weak plastic deformability at ambient temperature is commonly present in such RHEAs, resulting in poor processability during rolling and forging. Currently, it is imperative to seek some new strategies for enhancing the plasticity of RHEAs.

* Corresponding authors.
E-mail addresses: pliaw@utk.edu (P.K. Liaw), lhdai@lnm.imech.ac.cn (L. Dai).

https://doi.org/10.1016/j.jmst.2024.01.030
1005-0302/

Table 1
Experimental chemical compositions of these alloys studied (at.%).

Alloy	Al	Mo	Nb	Ti	B
BF	15.9	19.2	30.7	34.2	–
B15	15.0	18.5	30.9	34.4	1.2

Here, we developed the RHEA with multicomponent ceramic nanoparticles (MCNP-RHEA). In our strategy, the introduction of harder and more brittle borides (i.e., MCNPs) into the B2-type RHEAs $AlMoNb_2Ti_2$, departing from the traditional design philosophy, achieves unexpected plasticity. Generally, the most typical strategy to improve the plasticity of the matrix is to synthesize composites by adding ductile particles, such as metallic-glass composites [33]. Unlike the above, we demonstrate that the key to plasticity improvement in the present RHEAs lies in the ordering-to-disordering transition with the help of MCNPs. The chemical long-range ordered structure in the RHEA matrix was destroyed by high-density dislocations during deformation, which translates these local regions from the B2 to BCC structure. These disordered regions where the mobility of the dislocations is significantly increased near the MCNPs lead to the emergence of unique heterogeneous microstructures that further facilitate plastic deformation.

2. Materials and methods

2.1. Materials preparation

Ingots with nominal compositions of $(AlMoNb_2Ti_2)_{100-x}B_x$ ($x = 0$ and 1.5, in at.%) were prepared by arc-melting a mixture of these elements with purity higher than 99.9 weight percent (wt.%) in a Ti-gettered argon atmosphere. During preparation, the samples were flipped over and re-melted no less than eight times to ensure a homogeneous distribution of the alloying elements, and eventually drop-cast into a copper mold with a cavity of 3 mm in diameter and 70 mm in length. For convenience, the two alloys mentioned above will be labeled by their B concentrations, referred to as BF and B15, respectively.

Subsequently, a heat treatment was conducted at 1250 °C for 24 h to assuage elemental segregation due to rapid cooling. Before heating, all samples were covered with Ta foils and then sealed in a vacuumed quartz tube to minimize oxidation. After heat treatment, the tubes were removed from the furnace and the samples were cooled inside the vacuumed tubes down to room temperature. Long-duration annealing experiments at a high temperature of 1000 °C were conducted, using the same steps for up to 120 h. Alloy density was measured according to the Archimedes principle. The alloy composition was determined by inductively coupled plasma atomic emission spectroscopy (ICP-OES, Agilent 730) and is given in Table 1.

2.2. Mechanical tests

Room-temperature compressive tests were performed on a mechanical-testing machine (Lishi LE5105) at the strain rate of 1×10^{-3} /s and a strain gauge was employed to measure the deformation strain. The cylindrical samples were 3 mm in diameter and 4.5 mm in height, giving an aspect ratio of 1.5. Compression tests were performed at 600, 800, and 1000 °C in the same machine outfitted with a vacuum furnace and silicon-carbide platens. Before each test, the furnace chamber was evacuated to 10^{-4} torr. The samples were then heated to the test temperature at a rate of 20 K/min, and soaked at the test temperature for 15 min under 5 N load. These samples still exhibited a metallic luster after hot deformation, indicating that oxidation was effectively avoided during the testing.

Nanoindentation was performed on an Agilent Nano Indenter G200 with a Berkovich diamond tip to characterize the modulus and hardness. All indents were conducted, using a continuous stiffness method protocol to an indentation depth of 1000 nm. The average values collected at the indent depths of 500 to 600 nm are considered the modulus and hardness values obtained from one experiment.

2.3. Structures characterizations

Phase identification of the as-prepared samples was performed by X-ray diffraction (XRD, Rigaku Smart Lab) equipped with a monochromator. The crystallographic information was collected in the range of $2\theta = 20°–100°$ with a scanning speed of 2°/min. Microstructural characterization was conducted under scanning electron microscopy (SEM, JSM-7100F) equipped with electron backscatter diffraction detector (EBSD, an EDAX-TSL OIM system) and transmission electron microscopy (TEM, FEI Talos F200X) at 200 kV. EBSD images were acquired at a step size of 0.4 μm. In particular, the atomic-scale structure analysis was performed, employing Cs-corrected TEM, FEI Themis G2 300 at 300 kV. The dislocation analysis was conducted on the FEI Tecnai G2 operating at 200 kV. The in-situ tensile observation was conducted on FEI Talos F200X at a loading rate of 1 nm/s. The relative volume fraction of precipitates is statistically quantified on SEM images (at least five images) using the image processing software, MIPAR.

The samples for nanoindentation, SEM, and EBSD were prepared with a VibroMet 2 Vibratory Polisher. Their surfaces were ground using SiC papers (final grit size P3000) and the final polishing work was completed using active oxide polishing suspension (OPS) consisting of 50 nm colloidal silica. The samples used for dislocation analysis were processed by ion milling on Gatan 691. Other samples for the TEM observation were prepared by an FEI Helios NanoLab 600i Beam focused ion-beam (FIB) instrument.

Three-dimensional atom probe tomography (3D-APT) was performed with a Local Electrode Atom Probe (CAMECA LEAP 4000X Si) at a specimen temperature of 50 K, a detection rate of 0.8%, a pulse repetition rate of 200 kHz and an ultraviolet laser energy of 60 pJ in a laser-pulsing mode. Tip-shaped specimens for the 3D-APT tests were fabricated by a lift-out method and annularly milled in a FIB instrument. The estimated volumes of these samples before and after deformation were 1.87×10^5 and 1.10×10^6 nm^3, respectively. An Interactive Visualization and Analysis Software (IVAS™, version 3.8.2, CAMECA) was utilized to reconstruct the collected data and process the compositional analysis [34].

3. Results

3.1. Microstructure characteristics

Only BCC-type structures exist in the B-free (BF) RHEAs, while in B15 RHEAs, the BCC-type and orthorhombic structures appear, identified by XRD patterns (Fig. S1 in Supporting Information). In the B15 alloy, the weak peaks (marked by triangles) are related to the orthorhombic phase, whose structural characteristics are similar to those of TiB phases [35]. It is worth noting that in the B15 alloy (Fig. 1(a, b)), a large number of needle-like particles precipitate in the matrix, which are the aforementioned MCNPs. According to statistics, in the B15 alloy, the volume fraction of the needle-like particles is about 2%. It is determined that the grain sizes of BF and B15 alloys are 117.5 and 29.8 μm, respectively, based on the EBSD data analysis (Fig. 1(c, d)). With the introduction of a minor amount of B, the grain size of the alloy decreases significantly. This

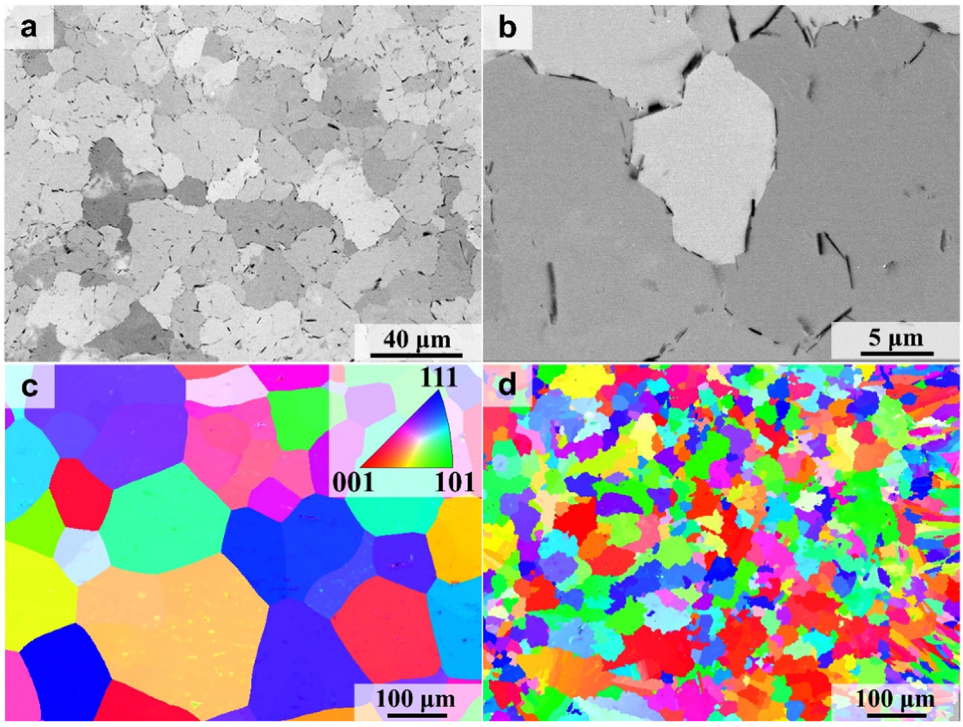

Fig. 1. Microstructure of BF and B15 alloys. (a) Backscatter electron (BSE) images of the B15 alloys. (b) Higher-magnification BSE images of the B15 alloys. (c, d) EBSD images of the BF and B15 alloys, respectively.

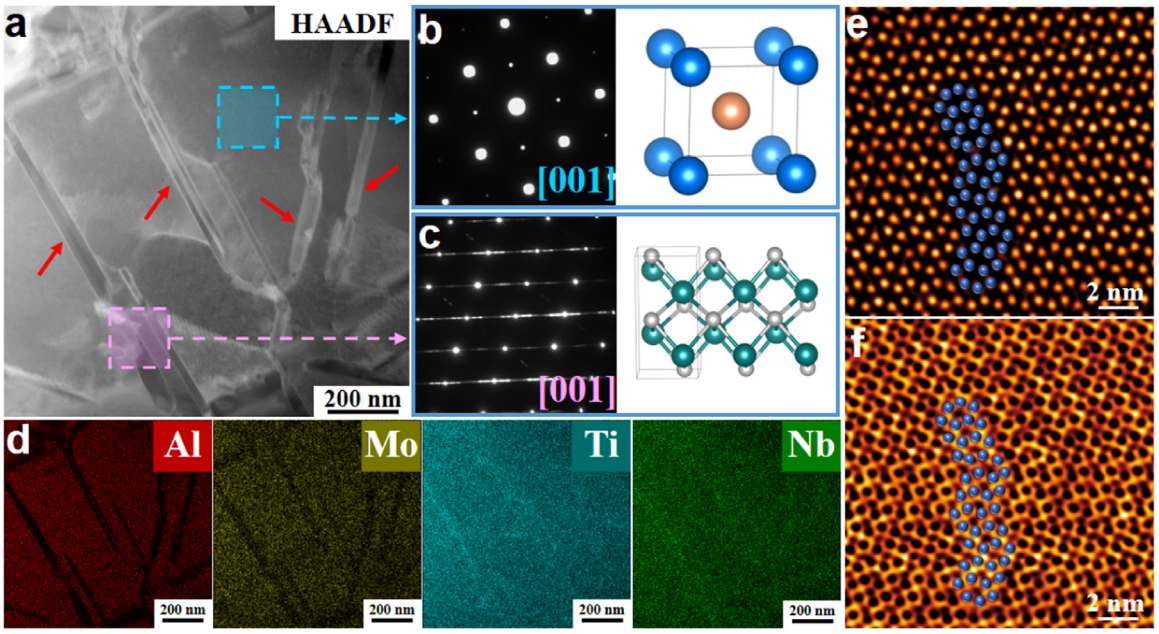

Fig. 2. Microstructure and elemental distribution of MCNPs in B15 alloys. (a) HADDF-STEM image showing the double-phase morphology. (b, c) The SAED and corresponding structural schematics of the matrix and precipitated phase, respectively. (d) EDS compositional maps showing the elemental distributions of each element, labeling different colors. (e, f) The HADDF and ABF micrographs of the MCNPs, respectively, showing the interface orientation of B27 [010]//BF[001].

is mainly because B acts as an inoculant to promote the heterogeneous nucleation process during solidification, which has been confirmed in other alloy systems [36,37].

The TEM characterization was conducted on the as-prepared samples to obtain more comprehensive crystallographic structure information. Fig. 2(a) represents a high-angle annular dark field (HADDF) image of B15 alloys. The selected area electron diffraction (SAED) patterns and corresponding structural schematics of the matrix and precipitated phase are presented in Fig. 2(b, c), respectively, which were collected from the zone axis parallel to [001]. The matrix phase can be determined to be a kind of ordered BCC structure, called the B2 structure, which is one of the variations of the BCC structure. The same ordered BCC structure is identified in the BF alloys (Fig. S2(a)). The precipitated phase has an orthorhombic structure, consistent with the XRD results (Fig. 1(a)). Compared with the matrix, Al and Mo atoms are largely depleted, while Ti and Nb are slightly enriched in the precipitated phases (Fig. 2(d)). Subsequently, the detailed phase composition and ele-

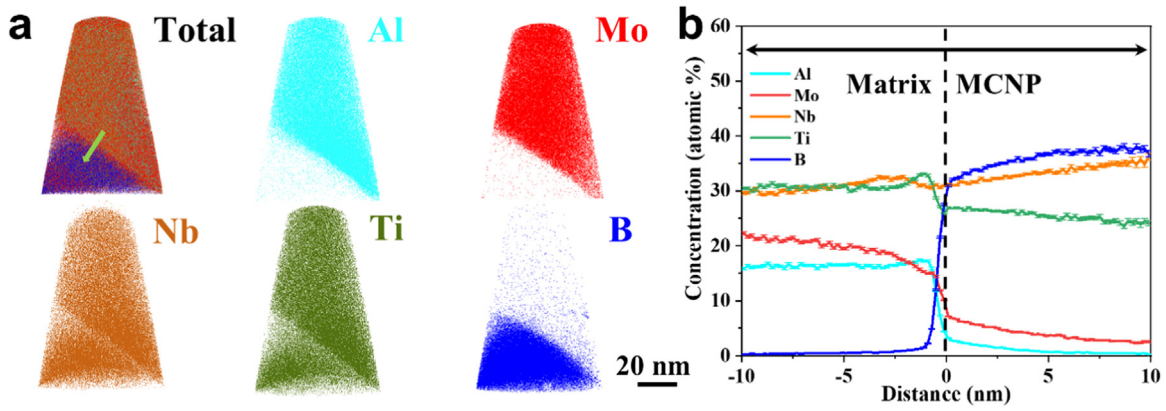

Fig. 3. (a) 2D reconstruction atom maps. (b) Proximity histogram across the matrix and MCNPs. The green arrow in (a) denotes the detected line across the matrix and MCNPs in (b).

mental distribution were investigated by 3D-APT (Fig. 3). From the two-dimensional (2D) reconstruction atom maps (Fig. 3(a)), it can be observed that the four elements of Al, Mo, Nb, and Ti are uniformly distributed in the matrix. However, in the MCNPs, the Al and Mo elements are significantly depleted, consistent with the observations in Fig. 2(d). The detailed compositions of the two phases can be read from the corresponding proximity histogram. It can be found that the solubility of element B in the matrix is about 0.1 at.%, while most of the boron is enriched in the MCNPs. Their crystal structure is the same as that of the TiB phases, but part of the Ti atoms is replaced by different proportions of Al, Mo, and Nb atoms, thus forming the characteristic multicomponent ceramic phase. The width of these borides is around 20–100 nm, analyzed from BSE microscopy and HADDF images. Remarkably, all diffraction spots are elongated into thin lines in the SAED of the MNCPs, demonstrating the existence of stacking faults [38].

To understand the stacking-fault mechanism more intuitively, the HADDF and annular bright-field (ABF) micrograph of the MCNPs are acquired under an aberration-corrected scanning transmission electron microscope (STEM) (Fig. 2(e, f)). It can be observed that B27 and BF structures have good compatibility, which is because the $(200)_{B27}$ planes fit excellently onto $(110)_{BF}$ planes, i.e., $(200)_{B27}//(110)_{BF}$ [39,40,41]. This fact makes it possible for the stacking disorder to occur. The HADDF-STEM micrograph of the B2 matrix phase is obtained (Fig. S2(b)), from which the lattice constant is statistically 0.3325 nm, slightly larger than 0.3252 nm obtained from the XRD analysis. In the B2 phases, obtained by the fast Fourier transformation (FFT), the diffraction spot of (100) planes can be verified, further proving the ordered structure (the inset of Fig. S2(b)). Based on the quantification of the Super-X EDS, the composition of the B2 matrix is 19.08Al-16.48Mo-30.24Nb-34.06Ti-0.14B (at.%), whereas that of the needle-like MCNPs can be regarded as 0.18Al-3.13Mo-24.75Nb-19.07Ti-52.87B (at.%).

Based on the above analysis, it is noteworthy that the crystal structure of the MCNPs is particularly analogous to those of TiB and NbB. These borides, belonging to the Topological Close-Packed (TCP) phases, generally exhibit a hard and brittle behavior due to the lack of an effectively movable slip system. The CALculation of PHAse Diagram (CALPHAD) calculations of the $(AlMoNb2Ti2)_{100-x}B_x$ alloys were developed using TCHEA3 databases via ThermoCalc software (Fig. S3). During the solidification of B15 alloys, the B2 phase is first precipitated in the metal liquid. Subsequently, the remaining liquid transforms into the MB phases with a B33 structure, in which M is a metal component. With further reduction of the alloy temperature, MB phases transform into the studied MCNPs. The polymorphic transformation common in Ti alloys (i.e., the $\beta \rightarrow \alpha$ transformation) will not continue to occur in the matrix because there are enough Mo and Nb atoms to inhibit the process.

3.2. Mechanical properties and thermal stability

The room-temperature compressive experiments of these alloys were then performed (Fig. 4(a)). At least five samples were tested for each composition. The BF samples have a yield strength (σ_Y) of 1085 ± 40 MPa, but a plastic strain of less than 5%. It does not exhibit obvious work-hardening behavior during deformation, and fracture occurs at 935 ± 50 MPa. It is a common phenomenon that most RHEAs with ordered structures usually present poor plasticity at room temperature [11,32]. Surprisingly, due to the introduction of appropriate MCNPs, the B15 samples show evident work-hardening behaviors, and their plasticity increases by about five times up to 23.5% ± 1.5%, compared with that of the BF samples. Not only has plasticity improved, but its strength has also exhibited a noteworthy increase, with a yield strength of 1380 ± 65 MPa and an ultimate strength of 1800 ± 30 MPa. As a brittle ceramic, the MCNPs are diffusely distributed in the alloy system with negligible deformability, which unexpectedly realizes the synchronous enhancement of strength and plasticity. Particularly, the enhanced plasticity in the RHEAs via brittle ceramic particles is an unusual phenomenon.

The Young's modulus and hardness of the B15 alloy are 171.4 and 6.71 GPa, and those of the BF alloy are 164.1 and 6.26 GPa, respectively, obtained by nanoindentation experiments. The density of the B15 alloy was measured to be about 6.48 g/cm^3, close to the density value of 6.46 g/cm^3 calculated by the rule of mixture (ROM), which is lower than those of traditional Ni-based alloys and most RHEAs. The stress–strain curves of BF and B15 alloys at high temperatures are presented in Fig. 4(b). The yield strengths of these alloys at different temperatures are listed in Table S2. With the increase of temperature, the yield strength of BF alloys gradually decreases, and are 700 ± 40, 670 ± 45, and 440 ± 50 MPa at 600, 800, and 1,000 °C, respectively. And the yield strengths gradually decrease, and are 1050 ± 50, 1000 ± 30, and 510 ± 65 MPa at 600, 800, and 1000 °C, respectively. At 1,000 °C, neither the BF nor B15 alloy fractures under compression. It is noted that the yield strength of B15 alloys remains above 500 MPa at 1000 °C. Based on the parameters of B15 alloys, the curve of the temperature dependence of the specific yield strength (the ratio of yield strength to density) is drawn (Fig. 4(c)). The thermally-activated, diffusionless dislocation glide changes to the diffusion-dominated dislocation slip or climbing at 0.5–0.6 T_m [8]. The temperature range of B15 alloys is about 830–1050 °C, as calculated by the ROM. Compared with the disordered RHEAs, B15 alloys with an ordered structure

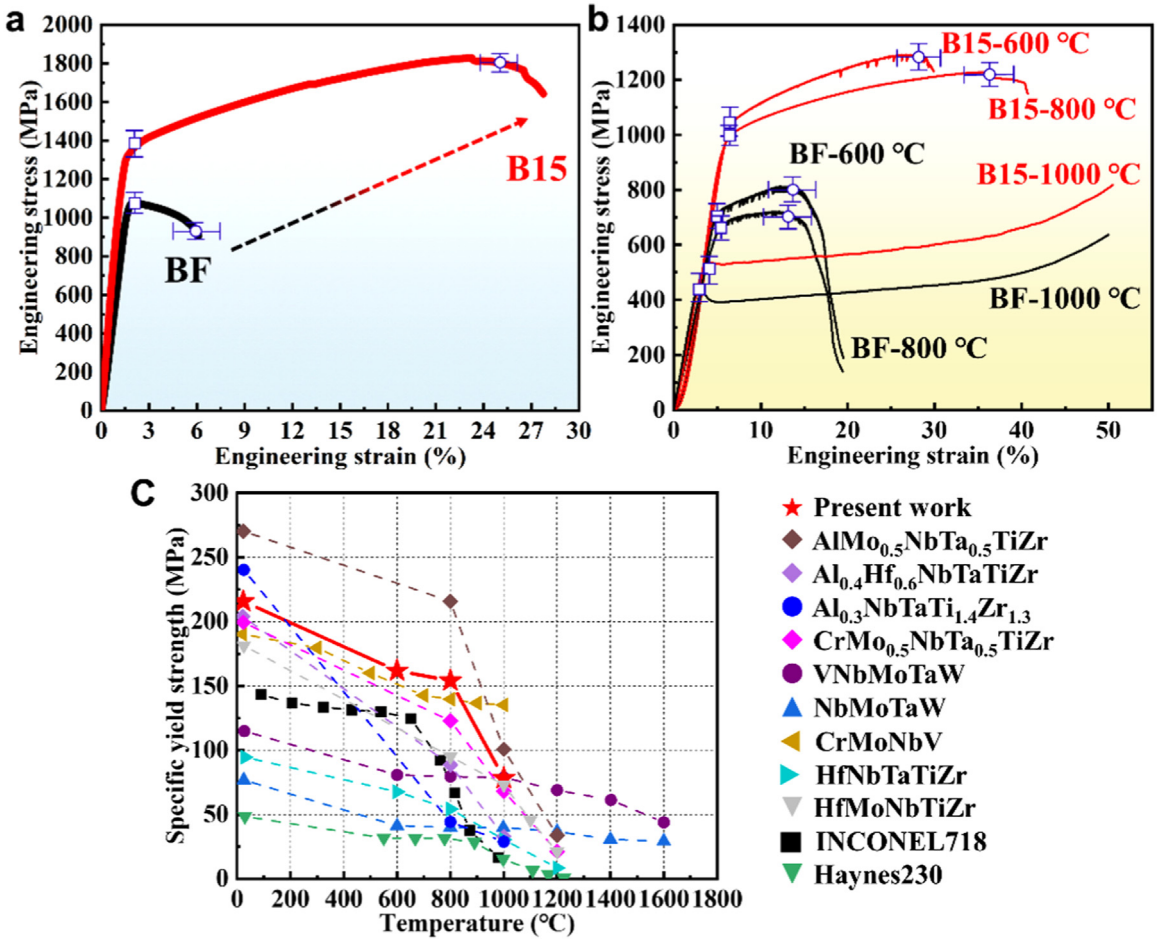

Fig. 4. Mechanical properties of BF and B15 alloys at different temperatures. (a) Stress–strain curves of two alloys at room temperature under compression. (b) Stress–strain curves of two alloys at high temperatures. (c) The temperature dependence of the specific yield strength in the B15 alloys, other typical RHEAs, and superalloys.

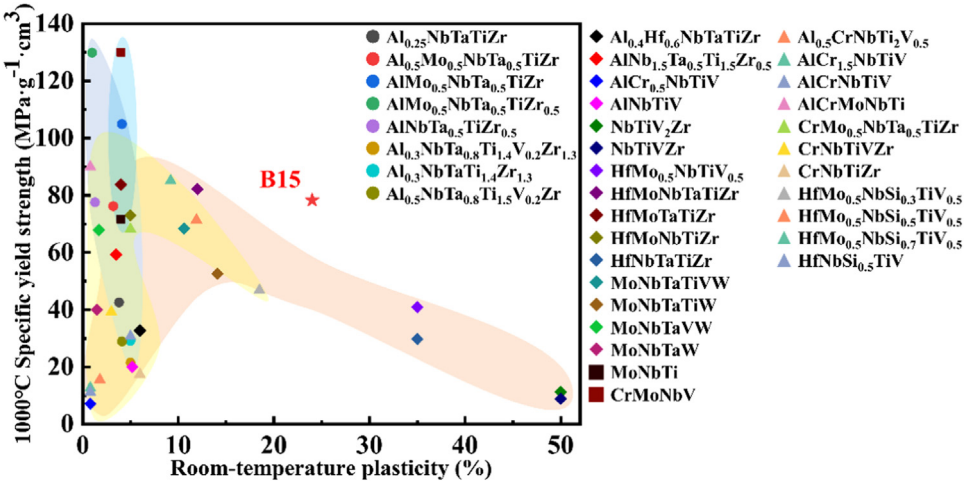

Fig. 5. Room-temperature plasticity vs 1000 °C specific yield strengths of representative RHEAs.

have stronger interatomic bonding, which makes them still stable at high temperatures and dislocation initiation insensitive to temperature.

The room-temperature plasticity vs 1000 °C specific yield strengths of representative RHEAs are summarized in Fig. 5 [1,42,43]. Although the available RHEAs all exhibit outstanding specific strengths at high temperatures, they almost all lack sufficient plasticity at room temperatures, and some of them do not even have high-temperature plasticity, which greatly limits their engineering applications [42]. It should not be ignored that for air/aero vehicles, reducing the density is an important way to improve energy conversion efficiency. At present, it is of great significance to develop RHEAs with both high-temperature specific strengths and room-temperature plasticity. Some RHEAs with only BCC structures, labeled by rhombuses and squares, have good room-temperature plasticity, but their high-temperature spe-

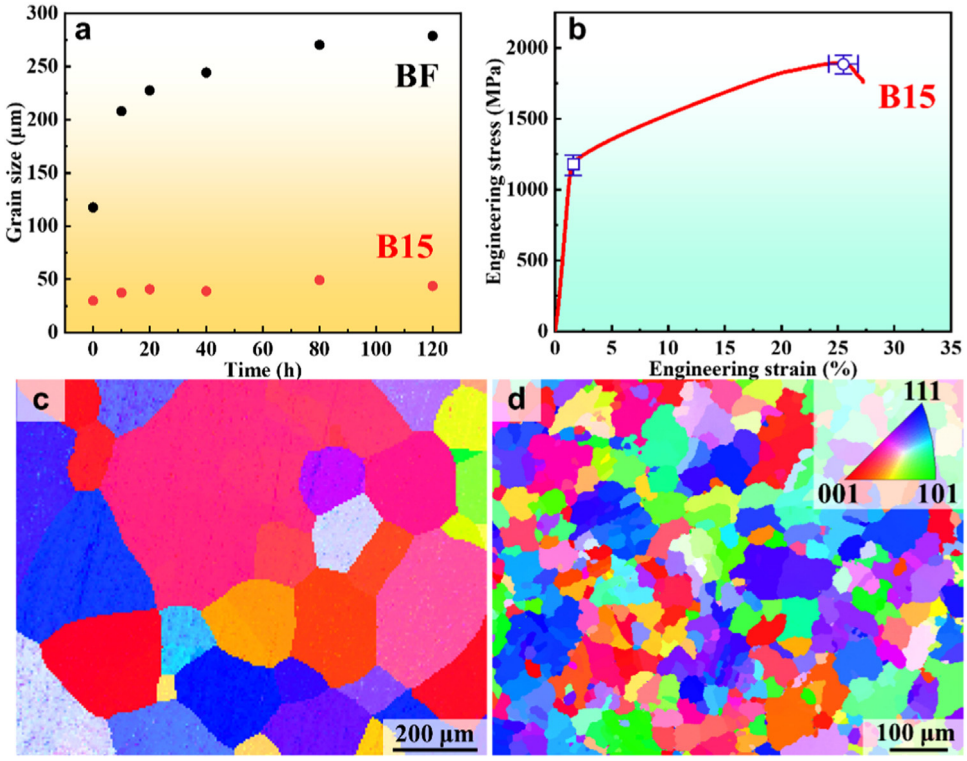

Fig. 6. Slow growth of grains at 1000 °C. (a) The variation of grain size as a function of annealing time. (b) Room temperature stress–strain curves of the B15 alloys annealed at 1000 °C for 120 h. (c, d) EBSD inverse pole figures for BF and B15 samples annealed at 1000 °C for 120 h, respectively.

cific strength is not sufficient. Other RHEAs with only BCC structures, represented by MoNbTi and CrMoNbV, possess high specific strengths at elevated temperatures, which is due to the mechanism of nonscrew-character dislocation-dominated deformation [1]. However, they maintain poor plastic deformability and still suffer from catastrophic fractures. The introduction of the TCP phases into RHEAs with BCC structures, labeled by triangles, significantly reduces its room-temperature plastic deformability. This indicates that it is particularly meaningful to suppress the formation of TCP phases or to regulate their size and distribution. RHEAs with B2 structures, labeled by circles, have almost no plastic-deformation behavior due to dislocation slip being limited by the superstructure [6]. Among this class of RHEAs, $AlMo_{0.5}NbTa_{0.5}TiZr_{0.5}$ exhibits the highest specific strength at 1000 °C, compared to all other refractory alloys. However, the present B15 alloy achieves a decent combination of strength and plasticity by introducing a moderate amount of MCNPs.

In the high-temperature service, the stability of the grain size is of vital importance for the mechanical properties. Hence, long-duration annealing was conducted in BF and B15 alloys at a high temperature of 1000 °C for 120 h (Fig. 6). It is well noticed that after annealing, the BF samples undergo significant coarsening, while the B15 samples remain almost constant (Fig. 6(c, d)). The MCNPs distributed near the grain boundary are believed to restrict the movement of the grain boundary by Zener pinning [44,45]. Compared with BF alloys, the migration rate of the grain boundary in B15 alloys is greatly limited by the existence of the MCNPs. Similar cases of improving grain stability by introducing borides have been reported in Ti alloys [44,46]. The stress–strain curve of the annealed B15 alloy is presented in Fig. 6(b). Its yield strength is 1,180 ± 60 MPa, with a plastic deformation of 24% ± 2%. Compared to the unannealed samples, the yield strength of this alloy has decreased by approximately 200 MPa, while the plastic deformability remains almost unchanged. This also indicates that the B15 alloy exhibits excellent thermal stability.

3.3. Microstructure deformed at room temperature

Fig. 7(a) represents the micromorphology of the B15 samples after 3% deformation at room temperature. It can be seen that a large number of dislocations, generated in the B2 matrix, pile up near the phase boundary between the MCNPs and B2 phases. The diffraction spots corresponding to the (100) superlattice can be seen to disappear in the range of approximately 300 nm near the phase boundary, from the SAED with the zone axis parallel to $[100]_{B2}$ (the inset of Fig. 7(a)). This result is likewise detected in the deformation area under the indentation (Fig. 7(d)). The disappearance of the diffraction spots suggests that the transition from ordering to disordering has occurred. It has been established that the diffraction intensity, I, is positively correlated with the structure factor, F, of a unit cell. Subsequently, F can be expressed as follows [47]:

$$F_{HKL} = \sum_{j=1}^{n} f_j e^{2\pi i(Hx_j+Ky_j+Lz_j)} \quad (1)$$

where HKL denotes the Miller indices of a given crystallographic plane, f_j the scattering factors for different sites in a unit cell. In crystals with BCC-type structures, there are generally two different sites occupied by atoms, namely the body-centered position (BP) and the vertex position (VP). Therefore, the expression for the structure factor, F, of the (100) plane can be written as [47]:

$$F = \left| f_{BP} - f_{VP} \right| \quad (2)$$

The magnitude of the scattering factor, f_j, is only related to the elements at the sites. In multicomponent alloys with chemically disordered structures, the possible atoms at BP and VP are random with equal probability. It implies that f_{BP} and f_{VP} are identical, meaning that the (100) planes do not form diffraction spots in the chemically-disordered alloy. The reason for the disappearance of diffraction spots can be explained clearly by the aforementioned

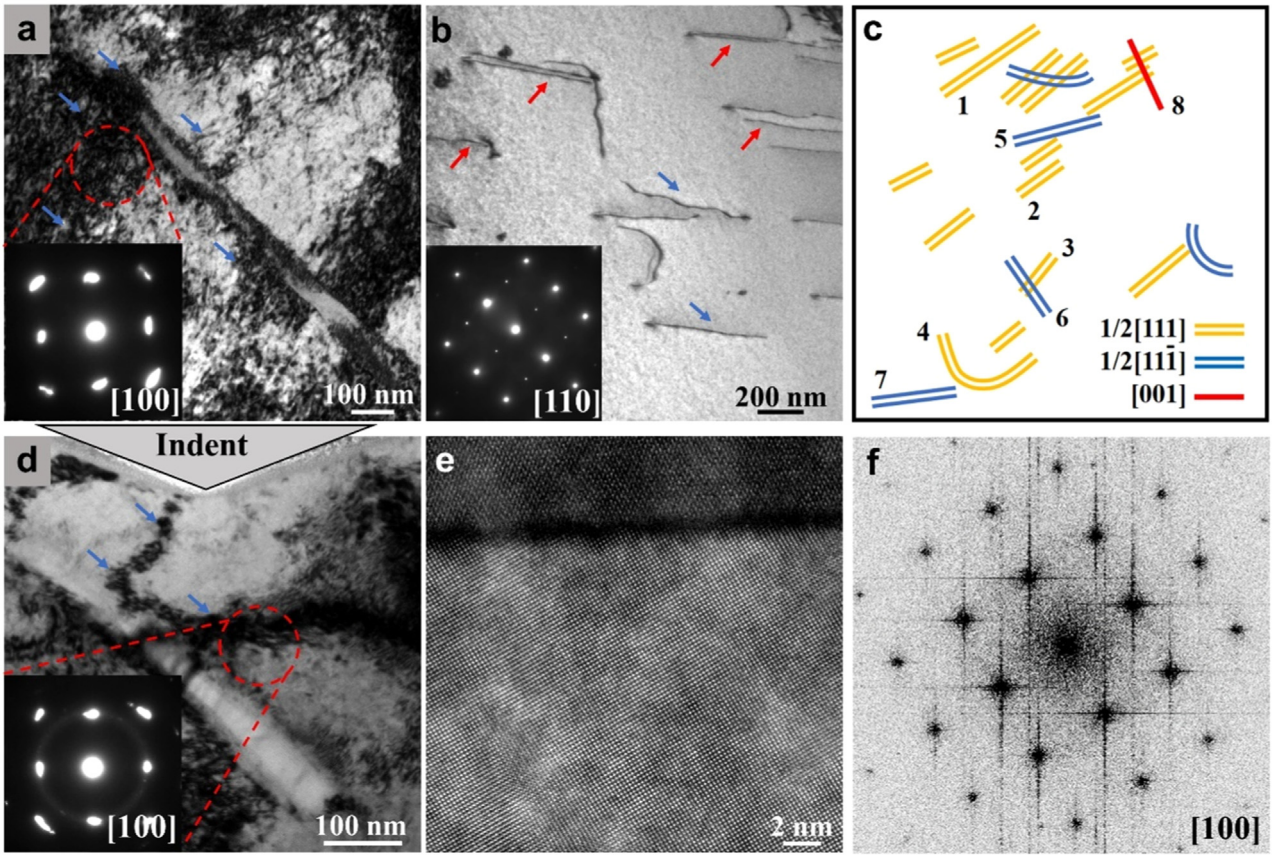

Fig. 7. Microstructure characterization of the B15 alloys after plastic deformation. (a) The micromorphology of the B15 alloys after 3% deformation at room temperature, and the insets are the SAED, showing a disordered structure. (b) TEM image at locations away from the MCNPs, and the insets are the SAED, presenting an ordered structure. (c) Schematic of the dislocations numbered 1 to 8 for the dislocation-line-direction analysis (The corresponding dislocation morphology is presented in Fig. S4 with different *g* vectors under two-beam conditions). (d) TEM image of the B15 alloys underneath indentation, illustrating the same disordered structure. (e) A high-resolution HADDF-STEM image near MCNPs, and (f) the associated FFT images.

theory from the perspective of physics. In the B15 alloys with ordered structures, these atoms near MCNPs move from BP to VP, or from VP to BP during the deformation process, contributing to the transition from ordering to disordering. This behavior may be caused by plastic deformation or dislocation glide.

To further confirm the fact, a random field in the vicinity of the phase boundary was selected for high-resolution HADDF-STEM observations (Fig. 7(e)). It can be concluded from the FFT image that there is no superlattice structure at the phase boundary of B15 alloys after deformation (Fig. 7(f)). Nevertheless, what is more intriguing is that the diffraction spots corresponding to the (100) superlattice do not disappear at locations away from the MCNPs, through the SAED with the zone axis parallel to $[110]_{B2}$ (the inset of Fig. 7(b)). It demonstrates that the ordered structure remains here, and the ordering-to-disordering transition occurs only in a small region around the MCNPs. The dislocation density in this field of view is much lower than that near the MCNPs. Moreover, some of the super dislocations, marked by red arrows, are observed to have undergone dissociation (Fig. 7(b)).

For further clarification of the mechanism of dislocation motion, the TEM observation was performed in the region away from the MCNPs under two-beam conditions. The BF TEM images of the B15 samples after 3% plastic deformation are presented in Fig. S4, which were taken under two-beam conditions along the zone axis of [001] or [$\bar{1}$13] with different *g* vectors. A substantial number of dissociated super dislocations are observed, consistent with the results in Fig. 7(b). Some of the dislocations are bent, which may be related to the interaction between dislocations and local compositional fluctuations [43]. The solute atoms on the pathway of dislocation movement play the role of pinning and make them bow out [48]. In addition, by comparing Figs. 7(a, b) and S4, an interesting phenomenon is found that the projection length of dislocation lines varies greatly near and away from MCNPs. The projection length of the former is only about 10 nm, while the projection length of the latter is almost more than 100 nm. Through the analysis of the invisibility criterion (Table S3), the Burgers vector, *b*, of the selected dislocation is defined (Fig. 7(c)). The dislocations with the Burgers vectors of 1/2[111] and 1/2[11$\bar{1}$] dominate the deformation process in the B15 alloy. A very small number of [100] dislocations, marked by #8 (Figs. 7(c) and S2(d)), are also detected in the upper right corner, which is formed through the interaction of <111> dislocations, common in the kind of B2 alloys, such as FeAl [49,50]. Subsequently, by the two-projection method with different zone axes [43], the line directions of the typical dislocations were analyzed, and the specific information is summarized in Table S4. Through the analysis of the relationship between the line direction and the Burgers vector on each dislocation, it can be found that all dislocations are of mixed character, i.e., there is no pure screw or edge dislocation. Compared with #4, #6, and #7, dislocations #1, #2, #3, and #5 have more screw character, because the angle between the line direction and the Burgers vector is close to 0. It can be proved that the movement of dislocations occurs mainly on the {110} and {123} planes in the B15 alloys, calculated from $\xi \times b$ (ξ refers to the line direction of each dislocation). The sufficiently small deviations are calculated as the angle between $\xi \times b$ and the slip plane.

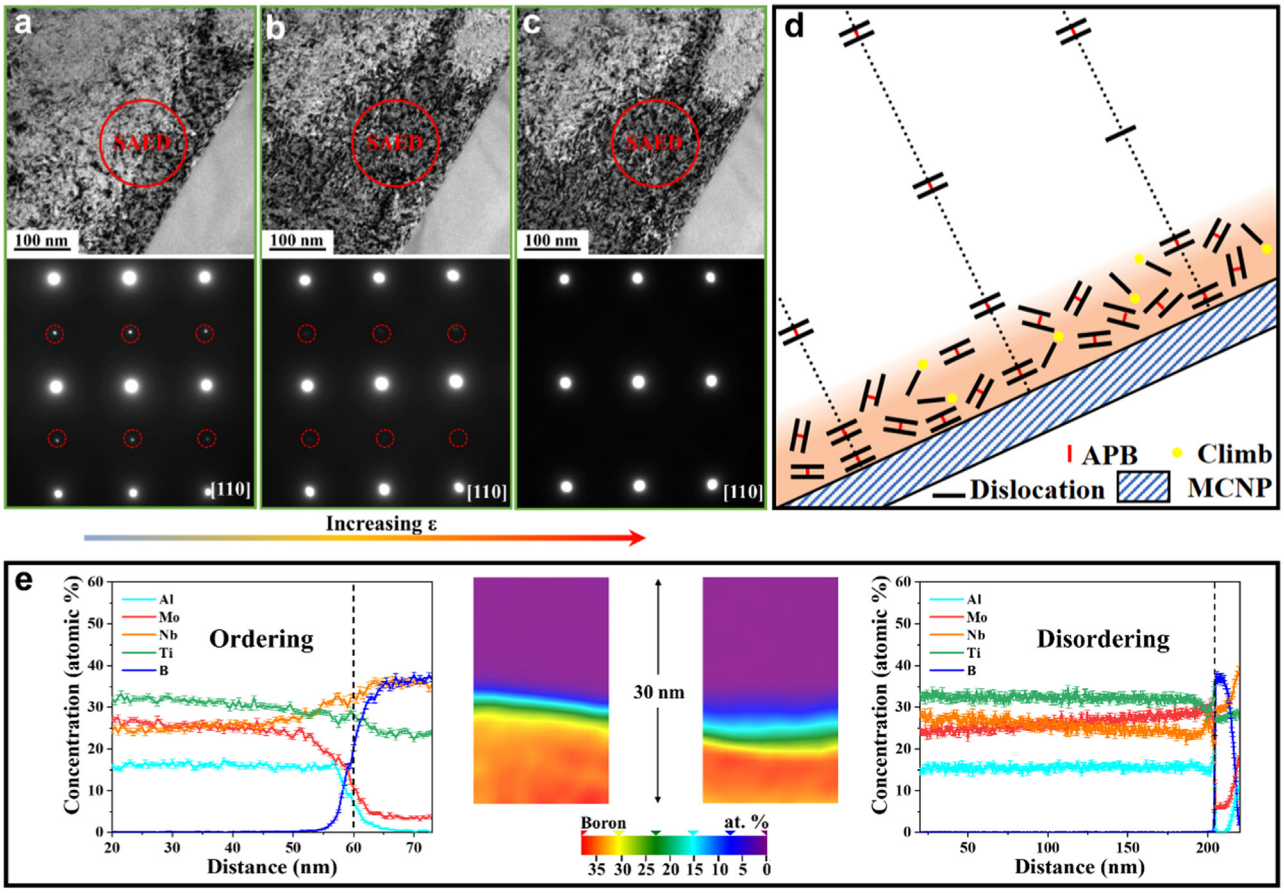

Fig. 8. Mechanism for the disordering behavior. (a–c) The step-by-step records at different moments of the deformation process in the in-situ tensile experiments, and corresponding SAED, respectively. (d) Schematic of the formation of the disordering process. (e) Proximity histogram of the ordered and disordered regions, and 2D-compositional contour maps revealing the elemental distribution of boron before and after deformation.

So far, the microstructure characteristics of the B15 alloy deformed at room temperatures are clear, which can be summarized as follows: i) the dissociated super dislocation dominates the plastic deformation; ii) all dislocations are of mixed character; iii) dislocation pileups exist near MCNPs, and iv) the transition from the chemically ordered B2 to disordered BCC phase occurs in the region near the phase boundary.

4. Discussion

4.1. Origin of the disorder

To clarify the underlying mechanism, it should be first demonstrated whether the transition from ordering to disordering is caused by plastic deformation or dislocation movement. Therefore, the in-situ tensile experiments of the B15 alloys were conducted with an in-situ loading device equipped with TEM (Fig. 8(a–c) and Movie 1). The step-by-step records at different moments of the deformation process are shown, operated along the *g* vector of [200] under the two-beam condition. By suspending the loading stress, the SAED was obtained at the moment corresponding to Fig. 8(a–c). With the increase in strain, the (001) superlattice reflection gradually disappears near MCNPs, which indicates that the structure factor, *F*, is decreasing. Furthermore, it is proved that the restrictions on the types of atoms are being weakened on body-centered and VPs. It can be seen (Fig. 8(c)) that the diffraction spots representing (001) planes no longer exist, which fully confirms that the intensification of strain enables the transition from ordering to disordering.

From the above evidence, it can be considered that the movement of dislocations in the process of plastic deformation promotes the transition. So, the dissociation behavior of super dislocations throughout the deformed B15 alloys was analyzed in detail. Generally, in BCC alloys, the Burgers vector of an ordinary dislocation is $a/2<111>$ (a denotes the lattice constant), which moves on the slip planes along the $<111>$ direction, that is, the distance of jumping one atom at a time [51]. However, the superlattice dislocation needs to move the distance of two atoms to maintain the ordered structure (the left part of Fig. 9(b)). Nevertheless, the movement of super dislocations to maintain the ordered structure is required to overcome great resistance, so it is difficult to occur. Naturally, these super dislocations are dissociated in the process of coordinated plastic deformation, which can be expressed as [51]:

$$a\langle 111\rangle = \frac{a}{2}\langle 111\rangle + \mathrm{APB} + \frac{a}{2}\langle 111\rangle \tag{3}$$

where APB represents an antiphase boundary. It can be seen that two partial dislocations I, II, and one APB tube constitute the existing form of dissociated super dislocations (Fig. 9(b)). Partial dislocations move only one atom's distance at a time, greatly reducing the resistance to slip, but it also promotes the emergence of APB, a local region of the chemical disorder [52]. This behavior is widely found in different ordered alloys through various characterization methods, such as Ti-6Al [53], Ni_3Al [54], and FeAl [55,56], and also appears in the B2-type RHEAs studied at present.

Fig. 9(a) displays the results of the inverse FFT (IFFT) in the B2 matrix of the B15 alloys with 3% deformation, selecting two {1 1 0} slip-plane reflections in the FFT pattern. It can be found that

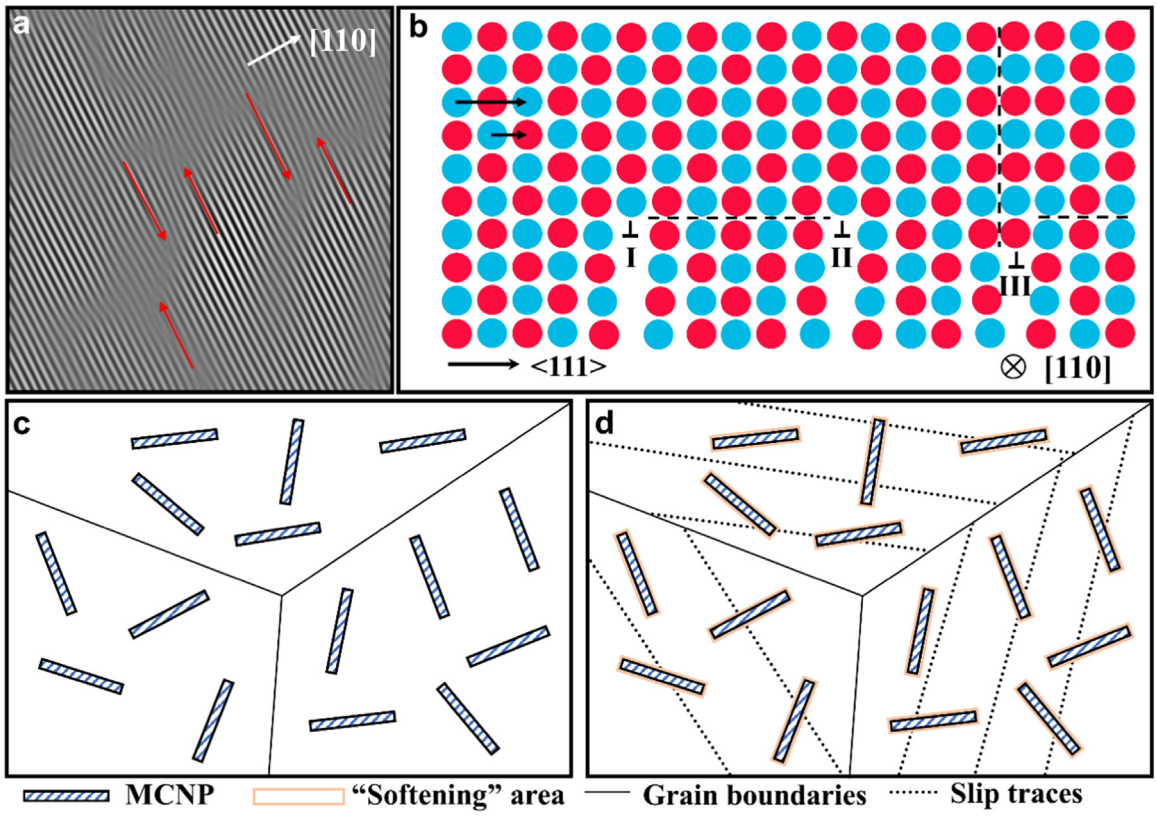

Fig. 9. Deformation characteristics of B15 alloys. (a) IFFT picture in the B2 matrix of the B15 alloys with 3% deformation, selecting two {1 1 0} (slip-plane reflections in the FFT pattern. (b) Schematic of the formation of APB. (c, d) The schematics of the microstructures before and after deformation, respectively, showing the special hard-softening-hard heterogeneous structure.

the semi-atomic plane of the dislocation with edge component is prevalent in the class of alloys, labeled by the red arrow. In the vicinity of these dislocations with edge components, misalignment or distortion of the atomic planes can be observed, which is the disorder of atomic arrangement caused by the formation of APB [55]. In addition, the interaction of dislocations and point defects can contribute to the occurrence of climbing. The behavior can also generate local chemical disorder, as presented by the dislocation III (Fig. 9(b)) [57]. In a word, the formation of APB tubes and climbing behavior in dislocation movement can lead to the local transition.

Why is the transition from ordering to disordering only realized near the MCNPs? The inhomogeneous deformation caused by the introduction of hard particles is mainly responsible for this phenomenon. Before and after macro yielding, the presence of geometrically necessary superlattice dislocations (GNSDs) coordinates the plastic deformation near the interface between B2 phases and MCNPs to inhibit the sprouting of microcracks [58]. These GNSDs continue to accumulate at the interface, accompanied by dissociation and climbing, and finally form a high-density dislocation region with a certain thickness (Fig. 8(d)). In the region, the increase in the APB density, induced by dislocation pileups, gradually makes the destruction of the ordered structure possible (Fig. 9(c, d)) [59]. Inhomogeneous deformation often leads to stress concentration and further dislocation accumulation at the interface [60,61]. It emphasizes that dislocation pileups are the reason for the transition. It is enough to explain why there is no transformation in the region away from MCNPs in the B15 alloys and the whole region of the BF alloys. In Refs. [54–56], after severe plastic deformation, such as high-pressure torsion (HPT), the superlattice-diffraction spots of intermetallics with a chemically ordered structure disappear under the TEM observation. The reason for the transformation is consistent with the present results, and it is also because the high density of dislocations leads to the accumulation of APB.

Moreover, the elemental distributions in the ordered and disordered regions are captured, respectively (Fig. 8(e)). From the one-dimensional (1D) compositional profile, there is no obvious difference in elemental concentrations near the interface before and after deformation. By comparing the 2D-compositional contour maps, it can be demonstrated that the elemental distribution of boron also does not change after deformation. In combination with the above analysis, the dislocation movement realizes the transition only by changing the local atomic occupation, while the long-range diffusion of elements does not occur during plastic deformation.

4.2. Mechanism for improvement of plasticity

It can be judged that the enhancement of plasticity of B15 alloys stems from the formation of the chemically disordered region near MCNPs, compared with BF alloys. Because it is the largest difference observed between them so far. To verify the hypothesis, the Kernel average misorientations (KAMs) for the B15 samples with deformations of 0%, 6%, 15%, and fracture are plotted (Fig. 10). It is widely accepted that the misorientations in different deformation stages can represent the approximate distributions of dislocations. In other words, the greater the misorientation, the higher the dislocation density at the position [62,63]. In Fig. 10(a), the green line denotes the low-angle grain boundaries, which also appear in Fig. 10(b, c), but are not obvious. With the increase of deformation, the overall dislocation density increases continuously. In particular, the red dots, regarded as a high-density dislocation area, are commonly found near the black dots that denote MCNPs. From the KAM picture of the fractured samples, it can be found more clearly

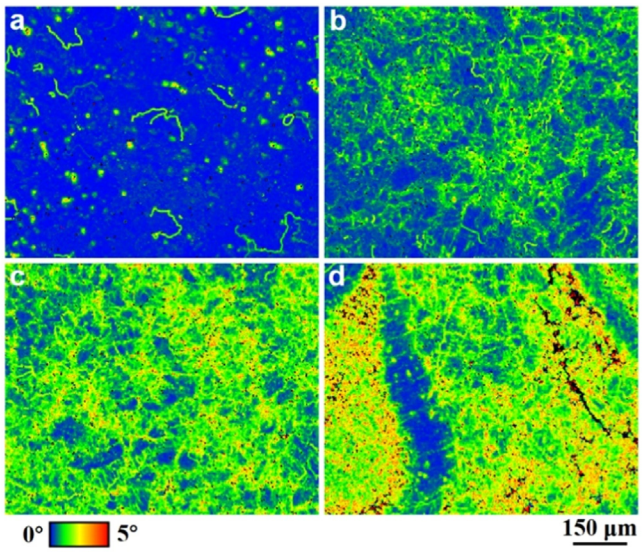

Fig. 10. KAM for the B15 alloys with deformations of (a) 0%, (b) 6%, (c) 15%, and (d) fracture respectively.

that high-density dislocations are clustered near MCNPs. But there are almost no dislocations responsible for plastic deformation in the place without MCNPs. The fact fully illustrates that the dislocation movement becomes more active at the interface between the two phases. The enhancement of the activity occurs exactly in the region of a deformation-induced disorder.

Compared with the disordered structure, the emission of dislocations needs to overcome the additional energy barrier in the ordered alloys [64,65]. When these dissociated super dislocations slip into the disordered region, the restraining effect of the APB energy on the partial dislocations is significantly reduced. Therefore, it is beneficial for the two partial dislocations to slip relatively independently. In addition, the reduction in the length of the Burgers vector, from the ordered structure of $a<111>$ to the disordered structure of $a/2<111>$, drives the decrease in the dislocation-slip resistance accordingly [57]. In short, in the disordered region, the movement of dislocations will be subject to less resistance and lower energy barriers required to overcome.

So far, it has explained why the introduction of hard and brittle TCP phases improves the plasticity of the B15 alloys abnormally. Although the MCNPs are very brittle, their existence creates many "softening" regions through the transition from ordering to disordering near the yield point. The "softening" does not mean that the strength of the region decreases, but that the mobility of these dislocations is significantly increased, compared to that of the ordered structure. Even if the volume fraction of MCNPs is only 2%, it is enough to improve the plastic deformability of the B15 alloys. It is mainly attributed to the fact that the MCNPs with nanometer width can achieve a ratio of surface area to volume large enough. More opportunities to form "softening" areas are available near these boundaries. However, the introduction of excessive B elements not only fails to improve plasticity, but also worsens it. In the B5 alloys (the concentration of B is 5 at.%), brittle fracture occurs, because the size of the ceramic particles reaches even the micron level (Fig. S5). It is not difficult to understand that in the B5 alloy, the increase in the number of B elements only leads to the coarsening of ceramic particles, and it cannot further trigger more "softening" areas. The experimental result coincidentally proves the rationality of the mechanism discussed at present from another perspective (that is, more boundaries introduce more "softening" areas). Special hard-softening-hard heterogeneous microstructures are built into the B15 alloy, as shown in Fig. 9(d), where the hard and brittle MCNPs are encapsulated by "softening" regions. These areas, acting as dislocation sources, improve the mobility of dislocation, effectively promoting homogeneous deformation, and further inhibiting the premature initiation of cracks.

4.3. Possibility of other mechanisms

It is known that grain refinement can generally improve strength without loss of plasticity. From the previous extensive experience, the refinement of grain sizes from hundreds of microns to dozens of microns could improve plasticity [66–68]. This reason can be attributed to the fact that more grains are involved in deformation, further reducing the possibility of stress concentration and promoting uniform plastic deformation. In the alloy system studied, the enhancement of plasticity is likely caused by the significant reduction in the grain size from BF to B15 alloys. However, the insight can be denied by the B015 alloy (the concentration of B is 0.15 at.%) as the control group. The B015 alloys with almost the same grain size as B15 alloys do not exhibit sufficient improvement in plasticity (Figs. S6 and S7). In the plastic-deformation stage, the softening of B015 alloys is slightly suppressed, compared to the BF alloys. These facts illustrate that grain refinement does promote homogeneous deformation and is not the underlying cause of the substantial increase in plasticity in the B15 alloys. From the perspective of inhibiting softening, compared with BF alloys, the introduction of brittle borides with nanoscale width does not aggravate the inhomogeneous deformation. On the contrary, more stable plastic deformations are achieved in the B15 alloys through the mechanism of the ordering-disordering transition near MCNPs.

Compared with the situation without the B element, the yield strength is increased by 295 MPa in the B15 alloys. This enhancement is not just due to grain refinement, and the additional improvement of strength in the B15 alloys can be attributed to i) the generation of GNSDs near MCNPs to accommodate strain incompatibility [37,41]; ii) load transfer from the B2 to MCNPs reinforcement through interfacial shear stresses (Load-sharing mechanism) [37,69,70].

The addition of the trace boron, as a small-size atom, tends to segregate at defects, such as grain boundaries and dislocations [71,72]. In the past few decades, the segregation of element B at grain boundaries has been recognized to enable a substantial increase in plasticity for intermetallics with ordered structures, especially Ni_3Al. In a recent study [73], boron was shown to increase the compression plasticity of inherently brittle NbMoTaW alloy. It is acknowledged that the segregation behavior improves the cohesive strength at the grain boundaries and fully restrains an intergranular fracture [73,74]. In B015 and B15 alloys, the same segregation-aggregation behavior is present. The B015 alloys exhibit modest plastic deformability compared to the BF alloys, indicating that the increase in the cohesive strength is beneficial for improving the plasticity in the present alloys.

5. Conclusions

In summary, the introduction of the MCNPs into the B2-type RHEAs enables simultaneous increases in both strength and plasticity. Compared with the BF alloys, the plasticity is increased by about five times up to 23.5%, and the yield strength is slightly increased to 1380 MPa in the B15 alloys. With the increase in temperature, its yield strengths at 600, 800, and 1000 °C are 1050, 1000, and 510 MPa respectively. In addition, due to the effect of Zener pinning, the grain boundary maintains high stability, and the grain size hardly changes after annealing at 1000 °C for 120 h.

The transition from ordering to disordering occurred in the vicinity of the MCNPs, observed in the in-situ TEM experiment. It

is explained in terms of the formation of APB tubes and climbing behavior driven by high-density dislocations. In these regions, as a sandwich between the B2 phases and MCNPs, the mobility of dislocations was detected to be remarkably enhanced, i.e., the initiation of "softening." The "softening" behavior occurs because the energy barrier required to overcome the emission of ordinary dislocations is lower than that of super dislocations. This unique heterogeneous structure within the B15 alloys adequately coordinates the plastic deformation and inhibits the premature occurrence of microcracks.

Author contributions

Lanhong Dai designed the research. Haiying Wang synthesized the series of materials and conducted mechanical tests. Hongyi Li, Fuhua Cao, and Tong Li performed TEM and in-situ TEM observation, respectively. Yan Chen, Haiying Wang, and Fuhua Cao conducted 3D-APT and EBSD analysis, respectively. Yuanyuan Tan, Hongyi Li, Peter K. Liaw, and Lanhong Dai analyzed the data and discussed the results. Hongyi Li, Yan Chen, Peter K. Liaw, and Lanhong Dai wrote the manuscript. All authors contributed to the comments and revisions of the manuscript.

Declaration of competing interest

The authors declare that they have no known competing financial interests or personal relationships that could have appeared to influence the work reported in this paper.

Acknowledgments

This research was supported by the Ye Qisun Science Foundation of National Natural Science Foundation of China (No. U2141204), the NSFC (Nos. 12102433 and 11972346), the NSFC Basic Science Center Program for "Multiscale Problems in Nonlinear Mechanics" (No. 11988102), the opening project of State Key Laboratory of Explosion Science and Technology (No. KFJJ23-03M). P.K. Liaw very much appreciates the support from the National Science Foundation (Nos. DMR-1611180, 1809640, and 2226508) with program directors, Drs. J. Madison, J. Yang, G. Shiflet, and D. Farkas and the US Army Research Office (Nos. W911NF-13-1-0438 and W911NF-19-2-0049) with program managers, Drs. M.P. Bakas, S.N. Mathaudhu, and D.M. Stepp.

Supplementary materials

Supplementary material associated with this article can be found, in the online version, at doi:10.1016/j.jmst.2024.01.030.

References

[1] F. Wang, G.H. Balbus, S. Xu, Y. Su, J. Shin, P.F. Rottmann, K.E. Knipling, J.C. Stinville, L.H. Mills, O.N. Senkov, I.J. Beyerlein, T.M. Pollock, D.S. Gianola, Science 370 (2020) 95–101.
[2] G.L. Zhao, H.Y. Qi, S.L. Li, Y. Liu, X.G. Yang, D.Q. Shi, Y.T. Sun, Adv. Mech. 52 (2022) 809–851.
[3] K. Pan, Y. Yang, S. Wei, H. Wu, Z. Dong, Y. Wu, S. Wang, L. Zhang, J. Lin, X. Mao, J. Mater. Sci. Technol. 60 (2021) 113–127.
[4] E.M. Francis, B.M.B. Grant, J.Q.D. Fonseca, P.J. Phillips, M.J. Mills, M.R. Daymond, M. Preuss, Acta Mater. 74 (2014) 18–29.
[5] S.T. Wlodek, Adv. Mater. Process. 162 (2004) 77.
[6] V. Soni, B. Gwalani, T. Alam, S. Dasari, Y. Zheng, O.N. Senkov, D. Miracle, R. Banerjee, Acta Mater. 185 (2020) 89–97.
[7] D.G. Leo Prakash, M.J. Walsh, D. Maclachlan, A.M. Korsunsky, Int. J. Fatigue 31 (2009) 1966–1977.
[8] O.N. Senkov, S. Gorsse, D.B. Miracle, Acta Mater. 175 (2019) 394–405.
[9] S. Naka, T. Khan, J. Phase Equilib. 18 (1997) 635.
[10] S. Naka, T. Khan, J.H. Westbrook, R.L. Fleischer, Intermetallic Compounds: Principles and Practice, John Wiley & Sons Ltd., New York, 2002.
[11] O.N. Senkov, J.K. Jensen, A.L. Pilchak, D.B. Miracle, H.L. Fraser, Mater. Des. 139 (2018) 498–511.
[12] Y. Chen, Y. Fang, R. Wang, Y. Tang, S. Bai, Q. Yu, J. Mater. Sci. Technol. 141 (2023) 149–154.
[13] D.B. Miracle, M.H. Tsai, O.N. Senkov, V. Soni, R. Banerjee, Scr. Mater. 187 (2020) 445–452.
[14] O.N. Senkov, D.B. Miracle, K.J. Chaput, J.P. Couzinie, J. Mater. Res. 33 (2018) 3092–3128.
[15] C. Lee, F. Maresca, R. Feng, Y. Chou, T. Ungar, M. Widom, K. An, J.D. Poplawsky, Y.C. Chou, P.K. Liaw, W.A. Curtin, Nat. Commun. 12 (2021) 5474.
[16] S. Wei, S.J. Kim, J. Kang, Y. Zhang, Y. Zhang, T. Furuhara, E.S. Park, C.C. Tasan, Nat. Mater. 19 (2020) 1175–1181.
[17] Z. Lei, X. Liu, Y. Wu, H. Wang, S. Jiang, S. Wang, X. Hui, Y. Wu, B. Gault, P. Kontis, D. Raabe, L. Gu, Q. Zhang, H. Chen, H. Wang, J. Liu, K. An, Q. Zeng, T.G. Nieh, Z. Lu, Nature 563 (2018) 546–550.
[18] B. Cantor, I.T.H. Chang, P. Knight, A.J.B. Vincent, Mater. Sci. Eng. A 375–377 (2004) 213–218.
[19] J.W. Yeh, S.K. Chen, S.J. Lin, J.Y. Gan, T.S. Chin, T.T. Shun, C.H. Tsau, S.Y. Chang, Adv. Eng. Mater. 6 (2004) 299–303.
[20] E.P. George, D. Raabe, R.O. Ritchie, Nat. Rev. Mater. 4 (2019) 515–534.
[21] Z. Li, S. Zhao, R.O. Ritchie, M.A. Meyers, Prog. Mater. Sci. 102 (2019) 296–345.
[22] Z. Li, K.G. Pradeep, Y. Deng, D. Raabe, C.C. Tasan, Nature 534 (2016) 227–230.
[23] Q. Pan, L. Zhang, R. Feng, Q. Lu, K. An, A.C. Chuang, J.D. Poplawsky, P.K. Liaw, L. Lu, Science 374 (2021) 984–989.
[24] M. Naeem, H. He, F. Zhang, H. Huang, S. Harjo, T. Kawasaki, B. Wang, S. Lan, Z. Wu, F. Wang, Y. Wu, Z. Lu, Z. Zhang, C.T. Liu, X.L. Wang, Sci. Adv. 6 (2020) eaax4002.
[25] Z. An, S. Mao, Y. Liu, L. Wang, H. Zhou, B. Gan, Z. Zhang, X. Han, J. Mater. Sci. Technol. 79 (2021) 109–117.
[26] S.P. Wang, J. Xu, J. Mater. Sci. Technol. 35 (2019) 812–816.
[27] Y. Jia, C. Ren, S. Wu, Y. Mu, L. Xu, Y. Jia, W. Yan, J. Yi, G. Wang, J. Mater. Sci. Technol. 149 (2023) 73–87.
[28] Y.Y. Tan, Z.J. Chen, M.Y. Su, G. Ding, M.Q. Jiang, Z.C. Xie, Y. Gong, T. Wu, Z.H. Wu, H.Y. Wang, L.H. Dai, J. Mater. Sci. Technol. 104 (2022) 236–243.
[29] X.J. Fan, R.T. Qu, Z.F. Zhang, J. Mater. Sci. Technol. 123 (2022) 70–77.
[30] Y.D. Wu, Y.H. Cai, T. Wang, J.J. Si, J. Zhu, Y.D. Wang, X.D. Hui, Mater. Lett. 130 (2014) 277–280.
[31] J.K. Jensen, B.A. Welk, R.A. Williams, J.M. Sosa, D.E. Huber, O.N. Senkov, G.B. Viswanathan, H.L. Fraser, Scr. Mater. 121 (2016) 1–4.
[32] O.N. Senkov, S.V. Senkova, C. Woodward, Acta Mater. 68 (2014) 214–228.
[33] D.C. Hofmann, J.Y. Suh, A. Wiest, G. Duan, M.L. Lind, M.D. Demetriou, W.L. Johnson, Nature 451 (2008) 1085–1089.
[34] Q. Chen, R. Hu, S. Jin, F. Xue, G. Sha, Acta Mater. 220 (2021) 117297.
[35] B.F. Decker, J.S. Kasper, Acta Crystallogr. 7 (1954) 77–81.
[36] B.S. Murty, S.A. Kori, M. Chakraborty, Int. Mater. Rev. 47 (2002) 3–29.
[37] G. Singh, U. Ramamurty, Prog. Mater. Sci. 111 (2020) 100815.
[38] B.J. Kooi, Y.T. Pei, J.T.M. De Hosson, Acta Mater. 51 (2003) 831–845.
[39] H. Feng, Y. Zhou, D. Jia, Q. Meng, Scr. Mater. 55 (2006) 667–670.
[40] K. Panda, K. Chandran, Acta Mater. 54 (2006) 1641–1657.
[41] M. Fang, Y. Han, Z. Shi, G. Huang, J. Song, W. Lu, Compos. Pt. B-Eng. 211 (2021) 108683.
[42] J.P. Couzinie, O.N. Senkov, D.B. Miracle, G. Dirras, Data Brief 21 (2018) 1622–1641.
[43] R. Feng, B. Feng, M.C. Gao, C. Zhang, J.C. Neuefeind, J.D. Poplawsky, Y. Ren, K. An, M. Widom, P.K. Liaw, Adv. Mater. (2021) e2102401.
[44] B. Cherukuri, R. Srinivasan, S. Tamirisakandala, D. Miracle, Scr. Mater. 60 (2009) 496–499.
[45] Z.K. Chen, X.Y. Li, Adv. Mech. 52 (2022) 397–409.
[46] T.M.T. Godfrey, A. Wisbey, P.S. Goodwin, K. Bagnall, C.M. Ward-Close, Mater. Sci. Eng. A 282 (2000) 240–250.
[47] D.B. Williams, C.B. Carter, Transmission Electron Microscopy: A Textbook for Materials Science, Springer Publication, 2009.
[48] G.P.M. Leyson, W.A. Curtin, Philos. Mag. 93 (2013) 2428–2444.
[49] A. Fraczkiewicz, B. Decamps, D. Colas, O. Calonne, F. Louchet, J. Alloy. Compd. 499 (2010) 176–182.
[50] P.R. Munroe, I. Baker, Acta Metall. Mater. 39 (1991) 1011–1017.
[51] A.H. Cottrell, Theory of Crystal Dislocations, Routledge, New York, 1964.
[52] C. Rentenberger, T. Waitz, H.P. Karnthaler, Phys. Rev. B 67 (2003) 094109.
[53] R. Zhang, S. Zhao, C. Ophus, Y. Deng, S.J. Vachhani, B. Ozdol, R. Traylor, K.C. Bustillo, J.W. Morris, D.C. Chrzan, M. Asta, A.M. Minor, Sci. Adv. 5 (2019) eaax2799.
[54] C. Rentenberger, C. Mangler, S. Scheriau, R. Pippan, H.P. Karnthaler, Mater. Sci. Forum 584–586 (2008) 422–427.
[55] C. Gammer, C. Mangler, H.P. Karnthaler, C. Rentenberger, Scr. Mater. 65 (2011) 57–60.
[56] D. Morris, M. Leboeuf, S. Gunther, M. Nazmy, Philos. Mag. A 70 (1994) 1067–1090.
[57] C. Rentenberger, H.P. Karnthaler, Acta Mater. 56 (2008) 2526–2530.
[58] D.A. Hughes, N. Hansen, D.J. Bammann, Scr. Mater. 48 (2003) 147–153.
[59] V.A. Starenchenko, O.D. Pantyukhova, S.V. Starenchenko, Phys. Solid State 44 (2002) 994–1002.
[60] Y.Y. Liu, P.Z. Liu, J.J. Li, P.K. Liaw, F. Spieckermann, D. Kiener, J.W. Qiao, J. Eckert, Int. J. Plast. 105 (2018) 225–238.
[61] D. Giuntini, S. Zhao, T. Krekeler, M. Li, M. Blankenburg, B. Bor, G. Schaan, B. Domènech, M. Müller, I. Scheider, M. Ritter, G.A. Schneider, Sci. Adv. 7 (2021) eabb6063.
[62] W. Pantleon, Scr. Mater. 58 (2008) 994–997.

[63] S.I. Wright, M.M. Nowell, D.P. Field, Microsc. Microanal. 17 (2011) 316–329.
[64] P.M. Anderson, J. Rice, Scr. Metall. 20 (1986) 1467–1472.
[65] T. Yang, Y.L. Zhao, W.P. Li, C.Y. Yu, J.H. Luan, D.Y. Lin, L. Fan, Z.B. Jiao, W.H. Liu, X.J. Liu, J.J. Kai, J.C. Huang, C.T. Liu, Science 369 (2020) 427–432.
[66] J. Liu, G. Zhu, W. Mao, S.V. Subramanian, Mater. Sci. Eng. A 607 (2014) 302–306.
[67] Q. Liu, G. Wang, X. Sui, Y. Liu, X. Li, J. Yang, J. Mater. Sci. Technol. 35 (2019) 2600–2607.
[68] S.J. Sun, Y.Z. Tian, H.R. Lin, X.G. Dong, Y.H. Wang, Z.J. Zhang, Z.F. Zhang, Mater. Des. 133 (2017) 122–127.
[69] V.C. Nardone, K.M. Prewo, Scr. Metall. 20 (1986) 43–48.
[70] A.M. Korsunsky, X. Song, J. Belnoue, T. Jun, F. Hofmann, P.F.P. De Matos, D. Nowell, D. Dini, O. Aparicio-Blanco, M.J. Walsh, Int. J. Fatigue 31 (2009) 1771–1779.
[71] D. Raabe, M. Herbig, S. Sandlöbes, Y. Li, D. Tytko, M. Kuzmina, D. Ponge, P.P. Choi, Curr. Opin. Solid State Mater. Sci. 18 (2014) 253–261.
[72] A.J. Detor, C.A. Schuh, Acta Mater. 55 (2007) 4221–4232.
[73] Z. Wang, H. Wu, Y. Wu, H. Huang, X. Zhu, Y. Zhang, H. Zhu, X. Yuan, Q. Chen, S. Wang, X. Liu, H. Wang, S. Jiang, M.J. Kim, Z. Lu, Mater. Today 54 (2022) 83–89.
[74] C.T. Liu, C.L. White, J.A. Horton, Acta Metall. 33 (1985) 213–229.